

# Tuning Hybrid Exciton-Photon Fano Resonances in Two-Dimensional Organic-Inorganic Perovskite Thin Films

*Franziska Muckel<sup>1,3\*</sup>, Kathryn N. Guye<sup>1</sup>, Shaun M. Gallagher<sup>1</sup>, Yun Liu<sup>1</sup>, and David S. Ginger<sup>1,2</sup>*

<sup>1</sup>Department of Chemistry, University of Washington, Seattle, WA 98195, USA

<sup>2</sup>Physical Sciences Division, Physical and Computational Sciences Directorate, Pacific Northwest National Laboratory, Richland, WA, 99352 USA

<sup>3</sup>Electroenergetic Functional Materials and CENIDE, University Duisburg-Essen, 47057 Duisburg

## **Corresponding Author**

\* Franziska Muckel: E-mail: [franziska.muckel@uni-due.de](mailto:franziska.muckel@uni-due.de)

**Abstract:**

As easy-to-grow quantum wells with narrow excitonic features at room temperature, two dimensional (2D) Ruddleson-Popper perovskites are promising for realizing novel nanophotonic devices based on exciton-photon interactions. Here we demonstrate a distinct hybrid exciton-photon Fano resonance in  $(\text{C}_4\text{H}_9\text{NH}_3)_2\text{PbI}_4$  thin films prepared via spin coating. Using a classical coupled-oscillator model and finite-difference time domain simulations, we link the Fano interference to the coupling of the exciton with the Rayleigh-like scattering of the film microstructure. Combining colloidal plasmonic cavities with the 2D perovskite films we demonstrate tuning of the Fano resonance. In combination with silver nanoparticles the exciton-photon Fano interference couples to the in plane plasmonic modes, with indications of Rabi splitting. By creating a Nanoparticle on Mirror geometry, we address the out-of-plane excitonic component, reaching an intermediate coupling regime. These structures suggest possible photonic targets for biomolecular self-assembly applications.

**Keywords:**

2D perovskites, Fano interference, light-matter interactions, plasmonics, strong-coupling, Butylammonium lead iodide

## Introduction:

Controlling light-matter interactions is crucial for the performance of optoelectronic devices. Owing to their strong absorption<sup>1,2</sup> and low trap densities<sup>3,4</sup>, lead halide perovskites (LHPs) have gained significant attention as active materials in both photovoltaics and light-emitting diodes<sup>5,6</sup>. LHPs can be synthesized with variable dimensionalities, displaying high oscillator strengths and large exciton binding energies.<sup>7</sup> Ruddlesden-Popper perovskites<sup>8</sup>, which self-assemble from solution as inorganic layers sandwiched between layers of intercalated alkylammonium cations, represent naturally grown quantum wells with large (>100 meV) exciton binding energies,<sup>9</sup> high oscillator strengths ( $0.7 \pm 0.1$ )<sup>10</sup>, and narrow linewidths (52 meV FWHM)<sup>11</sup> at room temperature. With these characteristics, low-dimensional perovskites have emerged as a promising platform for the tailoring of light-matter interactions. Effects like lasing<sup>12-14</sup>, enhanced absorption<sup>15</sup>, increased spontaneous emission<sup>16-19</sup>, and even Rabi splitting<sup>20-22</sup> have been demonstrated, which benefit both conventional optoelectronics<sup>23-25</sup>, and may open the path to novel devices like polariton lasers<sup>26</sup>, quantum sensing or optical computation applications.<sup>27,28</sup> Controlling distances in these systems is often of great importance, making them attractive targets for biomolecular self-assembly.<sup>29-32</sup> Fano resonances are particularly intriguing due to their applications in sensing, switching, and slow light devices.<sup>33-37</sup> A Fano resonance<sup>34-37</sup> is characterized by asymmetric spectral features and occurs due to the interference of a single, well-defined resonance with a continuum of states or another much broader mode. Originally developed to explain the asymmetric line shapes in the atomic spectra of helium,<sup>36</sup> its theory has been adapted to describe the spectral response in a variety of systems<sup>38-41</sup>, including coupling between excitons and plasmonic cavities<sup>42-45</sup>. An interesting aspect of LHPs is that, due to their high refractive index, they can act as optically resonant nanophotonic structures on their own, rendering additional cavities unnecessary. Different implementations range from Mie, Fabry-Perot or whispering gallery mode resonances in single nanostructures<sup>46,47</sup> to complex periodic structures such as photonic crystals<sup>48-51</sup>, metasurfaces<sup>52,53</sup> or photonic microlasers<sup>50,51</sup>. Recently, Franceschini et al. showed ultrafast modulation of a Fano resonance in optically resonant microparticles made of bulk-like CsPb(Br/Cl)<sub>3</sub><sup>54</sup>. However, the majority of resonant nanophotonic structures require complex synthetic strategies.<sup>27</sup>

Here, we study Fano resonances in 2D Ruddlesden-Popper butylammonium lead iodide ((C<sub>4</sub>H<sub>9</sub>NH<sub>3</sub>)<sub>2</sub>PbI<sub>4</sub>, BAPI) perovskite thin films prepared via spin coating. Using microscopic

darkfield scattering spectroscopy and finite-difference time-domain (FDTD) electrodynamic calculations, we find that the 2D excitonic transition, combined with a distinct grain-like microstructure, gives rise to a hybrid exciton-photon Fano interference. This Fano interference can be traced back to the coupling between the exciton and the scattering background caused by the dielectric material of the grain. Further, we investigated how this Fano resonance can be tuned by adding an additional plasmonic cavity. Near single silver nanoparticles, coupling with the exciton-photon Fano resonance of the 2D perovskites is observed, with indications of Rabi splitting in FDTD calculations. Using a particle-on-mirror geometry, we directly address the out of plane mode of the 2D perovskite exciton, achieving an intermediate coupling regime.

Figure 1a depicts an atomic force microscopy (AFM) image of the BAPI thin film prepared via spin coating, revealing its distinct microstructure. The 2D perovskite crystallizes in rectangular-shaped grains with thicknesses of about 10 nm to 25 nm and lateral dimensions of 150 nm to 1  $\mu$ m (cf. Figure S1). Figure 1b shows the photoluminescence (PL) and absorbance spectra from typical BAPI films on glass at room temperature. The PL spectrum exhibits a distinct peak at 520 nm, with a full-width at half-maximum (FWHM) of 17.5 nm (80 meV), consistent with previous reports for  $n=1$  BAPI.<sup>9</sup> The absorption spectrum depicts an excitonic peak at 512 nm and a step-like band onset around 535 nm, in good agreement with prior reports.<sup>9</sup> These results are consistent with large exciton binding energies in the 2D perovskite of  $>400$  meV.<sup>9</sup>

Scattering spectra on 2D perovskite films have not been commonly reported, although darkfield scattering is finding use as a probe of film degradation in 3D perovskites.<sup>55</sup> Figure 1c shows the darkfield scattering spectrum obtained under white light excitation (see Supporting Information for normalization). Surprisingly, the scattering spectrum exhibits an asymmetric shape, with a peak at 524 nm and a sharp minimum at 496 nm. Notably, the maximum shifts and broadens compared to the excitonic feature in PL (see Figure S2). The asymmetric scattering lineshape resembles that of a Fano resonance.<sup>36</sup> A common way to identify a feature as a Fano interference is by fitting with the Fano equation.<sup>37,56,57</sup> However, due to the strong curvature of the continuous background in the region of the interference, such fit only captures the spectral shape in the immediate vicinity (cf. Figure S3). In order to correct for the curvature of the background, we use that a Fano interference can be described with a coupled oscillators model, where only the oscillator with the larger damping is driven.<sup>37,58</sup> We describe the excitonic resonance as well as the

background with two classical, dissipative harmonic oscillators, coupled by the rate  $g$ . Following other work,<sup>59,60</sup> the shape of the scattering spectrum is given by:

$$\sigma_{scat} \propto \omega^4 \left| \frac{(\omega_{2D}^2 - \omega^2 - i\gamma_{2D}\omega)}{(\omega^2 - \omega_{2D}^2 + i\gamma_{2D}\omega)(\omega^2 - \omega_0^2 + i\gamma_0\omega) - \omega^2 g^2} \right|^2 \quad (1).$$

Here,  $\omega_{2D}, \gamma_{2D}$ , and  $\omega_0, \gamma_0$  represent the resonance frequency and damping of the excitonic resonance and the broader background, respectively. Figure 1c shows a fit of the scattering spectrum to the coupled oscillator model (red trace). Based on the fit of the coupled system ( $g > 0$ ), the uncoupled continuous background  $\sigma_0$  can be isolated mathematically (adjusting  $g = 0$ ), as shown in blue in Figure 1c. Figure 1d shows the normalized scattering spectrum (experimental data divided by  $\sigma_0$ ), which we fit with the normalized Fano equation (green line) to extract the Fano parameters ( $\epsilon = \frac{w-w_0}{\Gamma/2}$ , with  $w_0$  and  $\Gamma$  describing the resonance frequency and width)

$$\frac{\sigma_{scat}}{\sigma_0} = \left| \frac{q + \epsilon}{\epsilon + i} \right|^2 \quad (2)$$

The scattering data are well described by Eqn. 2, with  $q = -2.65 \pm 0.3$ , providing strong evidence that the optical feature observed in the scattering of BAPI thin film represent Fano resonance.

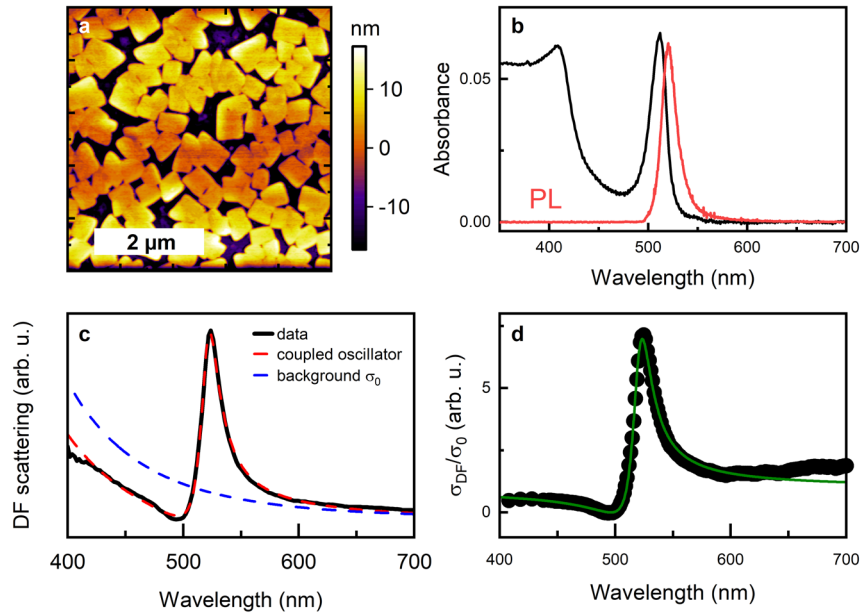


**Figure 1.** (a) Atomic force microscopy (AFM) image of a 2D perovskite thin films on glass. (b) Absorption and PL at 365 nm excitation of as-prepared 2D perovskite thin film on glass at room temperature. (c) Darkfield scattering spectrum of the 2D perovskite thin film at room temperature. The experimental data (black) is fit to a coupled-oscillator model (red dashed line). This allows

isolating the contribution of the unperturbed scattering background (blue dashed line). (d) Normalized darkfield scattering spectrum. The experimental data is divided by the scattering background  $\sigma_0$ . The green line represents a fit to a normalized Fano formula ( $E_0 = 2.386 \text{ eV}$  ( $519.7 \text{ nm}$ ),  $\Gamma = 0.086 \text{ eV}$ ,  $q = -2.65$ ).

Next, we investigate the broad scattering background causing Fano interference. In bulk-like  $\text{CsPb}(\text{Br}/\text{Cl})_3$  perovskite microcrystals, Fano interferences have been reported due to the coupling between the excitonic transition and Mie resonances supported by the microscopic structure of the material.<sup>54,61</sup> However, these structures have significantly larger dimensions ( $> 100 \text{ nm}$ ) in all three directions. To test whether the interference is related to the grain-like microstructure of the samples, we measured the material's full dielectric function using ellipsometry, and then performed FDTD simulations. Figure 2a shows the spectroscopic ellipsometry measurements of a 2D perovskite thin film. These traces were simultaneously fit with the transmission measurements (see Figure S4) to extract the complex dielectric function, shown in Figure 2b. We then performed FDTD simulations assuming a 20-nm-thick 2D perovskite layer located on top of a glass substrate embedded in a poly(methyl methacrylate) (PMMA) layer (see Supporting Information). Modeling the 2D perovskite as a continuous layer results in negligible scattering (see Figure S5). However, modeling the grain-like microstructure as a thin 2D perovskite cylinder with a diameter of  $\sim 150 \text{ nm}$  and a thickness of  $20 \text{ nm}$  (Figure 2c), produces a close-match to the experimental darkfield spectrum (Figure 1b). In addition, we reproduce the bare scattering stemming from a dielectric grain with a constant refractive index of 2.15 (baseline for the BAPI  $n$  value), shown in grey in Figure 2c. The spectrum resembles the mathematically deconvoluted background in Figure 1c. Based on these simulations, we conclude that the observed Fano interference occurs due to the coupling between the excitonic transition and the scattering caused by the film microstructure, and is best described as a hybrid photon-exciton Fano resonance. Note that no external cavity beside the perovskite grain itself is involved in the formation of the Fano resonance here, in contrast to previous works about Fano resonances in perovskite materials coupled to plasmonic cavities<sup>62,63</sup>.

Figure 2d depicts simulated scattering cross sections of BAPI grains with different diameters between  $300 \text{ nm}$  and  $700 \text{ nm}$ . The scattering amplitude scales with the grain size, while the spectral shape is conserved (grains with diameters  $> 40 \text{ nm}$  behave consistently, see Figure

S5b). These trends are in good agreement with our experimental results, which show no deviation in the spectral shape between grains from 150 nm to 1  $\mu\text{m}$  sizes. This result indicates that the observed hybrid Fano resonance is not influenced by small changes in layer morphology, as regularly occur with LHPs synthesized via spin coating. In a broader context, this hybrid exciton-photon Fano resonance related to the excitonic transition can be expected in the scattering spectrum of any 2D film which exhibits geometric structures causing Rayleigh scattering. This situation is the case in many 2D LHP samples prepared via spin coating.

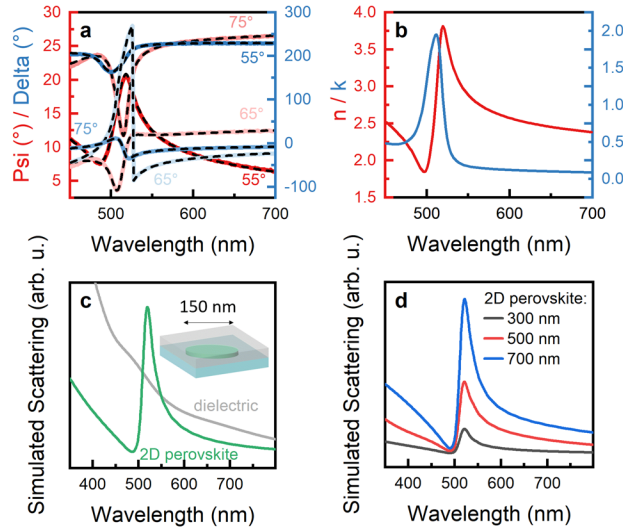


**Figure 2.** (a) Spectroscopic ellipsometry data and globally fitted model (dashed lines) for different incident angles of the light ( $55^\circ$ ,  $65^\circ$  and  $75^\circ$ ), measured on a BAPI thin film on glass at room temperature. (b) Refractive index and extinction coefficient of the 2D perovskite, as extracted from the ellipsometry measurements. (c) Simulated scattering spectrum (green line) assuming a cylindrical 2D perovskite grain. The grey line represents the scattering of a dielectric disk with the same dimensions and a constant refractive index of 2.15, providing a reference for BAPI without the excitonic resonance. The inset depicts a schematic of the FDTD model used for the simulations. The perovskite grains are modeled as a cylinder with a thickness of 20 nm and a diameter of 150 nm embedded in a matrix of PMMA (refractive index of 1.4) on a glass substrate. (d) Simulated scattering spectra for 2D perovskite grains with a thickness of 20 nm and different diameters of 300, 500 nm and 700 nm, all embedded in PMMA.

Next, we investigate how the hybrid exciton-photon Fano resonance can be addressed by coupling to plasmonic nanocavities. We synthesized silver nanoparticles (AgNP) – predominantly nanoprisms, truncated prisms and some nanodisks - in the size range of 15 nm to 50 nm exhibiting plasmon resonances centered around 480-520 nm following literature procedures (see Figure S6 for ensemble extinction and electron microscopy images).<sup>64,65</sup> We transferred the AgNPs from aqueous solution to hexane<sup>66</sup> and subsequently spin coated them on top of the BAPI, followed by the PMMA top layer (cf. Figure 3a). We adjusted the particle density on the film, allowing spectroscopic measurements of individual AgNPs.

Figures 3b-3c show darkfield scattering spectra typical of individual nanoparticles coupled to the BAPI film. All spectra exhibit two maxima and a minimum between 490 nm and 515 nm, correlated with the BAPI excitonic transition/hybrid Fano resonance. The single-particle spectra are corrected for the surrounding BAPI background (see Supporting Information). Figure 3b depicts representative spectra typical of about half the particles with relatively high darkfield scattering intensity and a large total width of the spectrum ( $>150$  nm/700 meV FWHM), where the reduction in the scattering amplitude at the excitonic position amounts for less than 50% of the maximum value. The spectral minima are between 510 nm and 516 nm. The asymmetric spectral shape identifies these spectra as Fano dips, indicative of an intermediate coupling regime. We hypothesize these spectra are associated with larger particles with less defined geometries or potentially small agglomerates. The other half of the particles exhibit more distinct dips in the spectrum reaching the baseline, as depicted in Figure 3c. These spectra exhibit a distinct maximum at around 520 nm, which seems to be related to the BAPI exciton-Fano resonance. The high energy maxima are found to shift between different spectra, while the minima are located between 494 nm and 502 nm. To eliminate the possibility that those spectra are superpositions of uncoupled BAPI with resonance peaks of AgNPs, we fabricated samples with inverted geometry (Figure 3d), allowing us to compare the darkfield scattering of specific individual AgNPs as bare particles on glass and coupled to the BAPI. Figure 3e and f depict darkfield scattering of two individual AgNPs before (blue) and after deposition of the BAPI layer (red). The spectra of bare particles depict linewidths of 209 meV and 211 meV, consistent with single particles. The spectra of the coupled system resemble those assorted in Figure 3c, deviating from a simple superposition (cf. Figure S7).

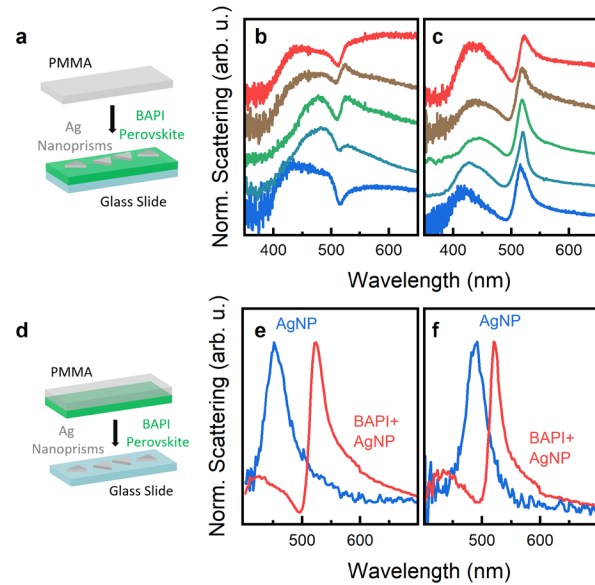


**Figure 3.** (a) Schematic illustration of the sample architecture for the coupled nanoparticle-perovskite system. (b, c) Darkfield scattering spectra of individual nanoparticles coupled to 2D perovskites. (d) Schematic illustrating the sample stacking for the inverted nanoparticle-perovskite system. (e, f) Single AgNP darkfield scattering spectra of two different individual AgNP on glass without (blue) and after covering with a 2D perovskite layer (red) and PMMA.

To gain more insight into the nature of the coupling, we conducted FDTD simulations of the coupled system (see Figure 4). While a splitting in scattering can arise in both regimes, a Fano interaction or a Rabi splitting, mode splitting in the absorption signal is usually taken to unambiguously indicate strong coupling.<sup>67–69</sup> As absorption on single particles is difficult to obtain, simulated absorption has often been used to distinguish between intermediate and strong coupling for a specific emitter-cavity combination.<sup>70–74</sup> Here we model the AgNPs as nano disks using the Palik optical constants for Ag,<sup>75</sup> to give a lower estimate of the coupling strength as compared to nanoprisms with electric field enhancement at the edges. First, we analyzed the coupling between the BAPI exciton and the AgNPs, neglecting the microstructure of the 2D perovskite by modeling the BAPI as a continued layer. Figure 4a and b depict the scattering of the combined system as well as the absorption of the AgNP coupled to the BAPI for AgNPs of different sizes. The spectra of the uncoupled AgNPs embedded in a dielectric of  $n=1.4$  on glass are shown as reference in grey. For all particle sizes, the spectra of the coupled system display a splitting with a minimum at around 513 nm/515 nm for absorption and scattering, respectively. We thus conclude that those AgNPs with high scattering amplitude directly couple to the exciton

of the 2D perovskite. Next, we include the microstructure in our simulation. The total scattering spectra of the coupled system becomes dominated by the spectral features of the BAPI exciton-photon Fano resonance, with shoulders indicating the contribution of the plasmonic particles (see Figure S8b). It resembles the raw experimental data well, as obtained prior to the subtraction of the BAPI background (see Figure S8). Figure 4c depicts the simulated absorption spectra of the AgNP coupled to BAPI grain, revealing a splitting with a profound dip shifted to 506 nm, roughly coinciding with the position observed in experimental scattering spectra with lower intensities (Figure 3c,e and f). This result suggests that the spectra in Fig 3c, e-f evidence coupling between the AgNP and the hybrid exciton-photon Fano resonance. It indicates that strongly scattering particles directly couple with the excitonic emitter, while for particles with smaller scattering cross-sections and less intense scattering, the scattering due to the microstructure dominates the line shape. To estimate the coupling regime in the system, we extracted the spectral positions of the two maxima in the simulated scattering (blue) and absorption (green) spectra for AgNPs of different sizes, revealing a splitting of  $\Omega = 387 \text{ meV}/350 \text{ meV}$ . This value exceeds the mean linewidth of the AgNPs measured in single particle spectra of  $\gamma_p = 202 \pm 11 \text{ meV}$  as well as the linewidth of the 2D perovskite ( $\gamma_{2D} = 55 \pm 11 \text{ meV}$  among all fits in this work), fulfilling the requirements for strong coupling  $\Omega > \gamma_p, \gamma_{2D}$ . Together with the observed splitting in the simulated absorption spectra (Figure 4a and c), this value of the Rabi splitting indicates, at least in our simulations, the BAPI is strongly coupled to AgNPs. Although strong coupling is not the main focus of the present study, these results nevertheless indicate that Rabi splitting between the hybrid exciton-photon Fano resonance and the AgNP plasmon is likely occurring in this system with realistic sample properties, although final experimental evidence e.g., through photoluminescence splitting cannot be observed here due to the strong signal of the surrounding BAPI.

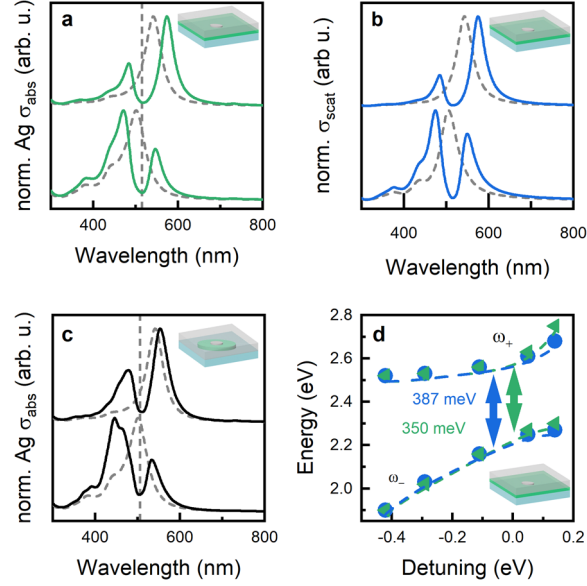


**Figure 4.** (a) Simulated absorption caused by the Ag nanodisks within the AgNP - 2D perovskite system: Ag nanodisks with different sizes (30 nm and 40 nm from bottom to top) placed on a uniform layer of 2D perovskite embedded in PMMA. (b) Simulated scattering spectra of the AgNP - 2D perovskite systems. Grey spectra in (a) and (b) depict the scattering or absorption spectra, respectively, of the uncoupled Ag nanodisks embedded in a dielectric material with refractive index of 1.4 on glass. (c) Isolated AgNP absorption of Ag nanodisks with a 20 nm (bottom) and 30 nm (top) diameter on top of a 150 nm diameter BAPI grain placed on glass and embedded in PMMA. Simulations in b and c are compared to experimental data from Figure 3 in Figure S11. (d) Detuning plot extracted from the maxima in the scattering and absorption spectra of Ag nanodisks with different sizes (4a and b among others), placed on a uniform layer of 2D perovskite embedded in PMMA (see (a-b)). The detuning value is determined as the difference between the medium peak position of the scattering of uncoupled AgNP and the energetic position of the dip in the scattering of coupled particles (2.401 eV). Dashed lines are guides to the eye.

Finally, we turn to explore the out-of-plane mode of the excitonic transition by modifying our sample geometry using a particle-on-mirror design,<sup>76</sup> evaporating a chromium/gold layer prior to spin coating of the BAPI (cf. Figure 5a). In this architecture, the out-of-plane plasmon mode in the nanoparticle couples with mirror charges induced in the gold film, giving rise to a vertically-coupled plasmon mode. In contrast to III-V or II-V quantum wells, transitions with out-of-plane

polarization are not forbidden in 2D halide perovskite materials. While the main extinction peak for level AgNPs is defined by the in-plane dipole resonance mode,<sup>77</sup> the dominant resonances in particle-on-mirror geometries are known to stem from out-of-plane modes.<sup>76</sup> Using unpolarized white light as the darkfield excitation source, we are able to excite modes polarized in both directions.<sup>76</sup> Compared to the bare AgNP, the AgNP-on-mirror cavities exhibit broader resonance peaks in single particle darkfield scattering, which are slightly shifted to the red (cf. Figure S9). In combination with the BAPI 2D perovskite, the spectra exhibit a pronounced peak splitting with a spectral dip at around 515 nm, compare Figure 5c and d. As the scattering of the AgNP-on-mirror plasmonic system is significantly more intense than the BAPI scattering, we expect the cavities to couple directly to the exciton. Indeed, the observed spectra can be well described with a two-oscillator model (red dashed lines in Figure 5c and d), with one oscillator representing the excitonic transition of 2D perovskite ( $\omega_{2D}, \gamma_{2D}$ ) and the other the plasmonic resonance ( $\omega_p, \gamma_p$ , replacing  $\omega_0, \gamma_0$  in Equation (1)). Fits to 14 different single particle darkfield spectra reveal a mean coupling strength  $\Omega = 2g$  of  $327 \pm 56$  meV. Figure 5b depicts the spectral position of the two maxima ( $\omega_{\pm}$ ) as well as the minimum, which relates to the spectral position of the BAPI excitonic transition ( $\omega_{2D}$ ), for the different spectra in relation to the detuning  $\delta = \omega_p - \omega_{2D}$  ( $\omega_p$  is calculated based on the knowledge of  $\omega_{2D}$ ,  $\omega_+$  and  $\omega_-$ )<sup>78</sup>. To extract the coupling strength, the spectral positions of the upper and lower branch of two coupled oscillators can be described within the quantum mechanical Jaynes-Cummings model (provided  $\gamma_{2D} \ll \Omega$ ):  $\omega_{\pm} = \frac{1}{2}(\omega_{2D} + \omega_{pl}) \pm \frac{1}{2}\sqrt{\delta^2 + \Omega^2}$  (3). We fit the experimental data in Figure 5b to obtain a coupling strength of 284 meV, in fair agreement with the value estimated by fitting the spectra directly. Although the coupling strength is in the same order of magnitude as the estimated coupling strength for the in-plane mode of the bare AgNPs, the system remains in the intermediate coupling regime due to the increased linewidth of the AgNP-on-mirror plasmonic cavity (mean value among the two-oscillator fits accounts for  $\gamma_p = 472 \pm 92$  meV). This characterizes the spectral feature observed in the spectra of AgNP-on-mirror cavities coupled to BAPI as intermediate coupling rather than Rabi splitting.

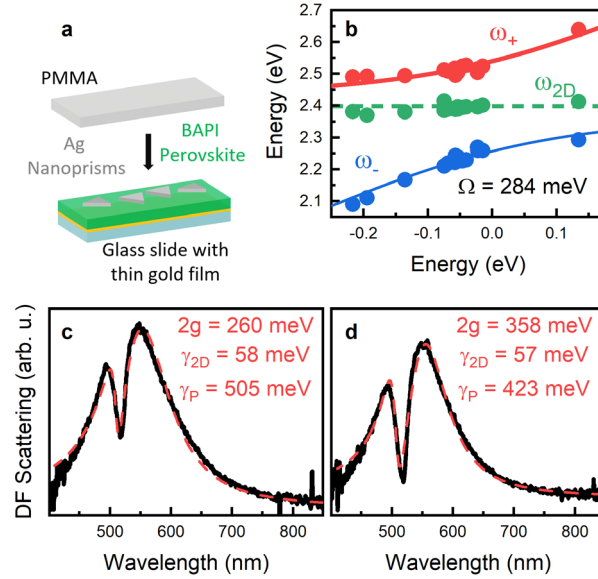


**Figure 5.** (a) Schematic illustrating the sample architecture for the AgNP-on-mirror system. (b) Energetic position of the lower maximum ( $\omega_-$ ), upper maximum ( $\omega_+$ ) and dip ( $\omega_{2D}$ ) in the spectra of individual AgNP-on-mirror. The red and blue line represent fits to a Jaynes-Cummings model. (c, d) Single particle darkfield spectra of individual AgNP-on-mirror cavities. Red dashed lines depict coupled oscillator fits to the data.

In conclusion, we have characterized scattering resonances in 2D halide perovskite films, both in isolation and when coupled to plasmonic cavities. This work not only confirms the potential of 2D perovskite quantum wells as excitonic materials in resonant nanophotonics, but also underlines the importance of accounting for the film microstructure when considering 2D perovskites for photonic or optoelectronic applications. We show that the coupling between the scattering generated by the grain-like structure of the BAPI and the strongly -bound excitonic transition gives rise to a pronounced exciton-photon Fano resonance, which can alter the light-matter-interactions drastically. In combination with plasmonic cavities we demonstrate tuning of this resonance. The comparison between different emitter-cavity systems indicates that the impact of the microstructure-related Fano interference depends on the optical cross-section of the coupled cavity resonator. Even though our findings were obtained on samples specifically designed to exhibit a high degree of microscopic inhomogeneity, they have broader importance for the usage of 2D perovskites coupled to cavities in general. 2D perovskite layers of any thickness prepared via spin

coating crystallize in grains with boundaries which inherently cause scattering, therefore the excitonic features cannot be fully decoupled from the structural optical properties. Thus, the impact of the microstructure on the optical properties of coupled 2D-perovskite-emitter-cavity systems need to be considered.

## AUTHOR INFORMATION

### **Corresponding Author**

\* Franziska Muckel: E-mail: [franziska.muckel@uni-due.de](mailto:franziska.muckel@uni-due.de)

### **Present Addresses**

Franziska Muckel - Elektroenergetic Functional Materials, University Duisburg-Essen, Bismarckstraße 81, 47057 Duisburg, Germany

## SUPPORTING INFORMATION

- Synthesis of AgNP, sample preparation, optical characterization, ellipsometry measurements, structural characterization, FDTD simulations, AFM topography, comparison of DF and PL spectra, Fano fit to uncorrected DF scattering, extinction and SEM of AgNP, extraction of AgNP scattering spectrum, uncoupled plasmonic cavities, Rayleigh fit to background, comparison of FDTD and experimental data.

## ACKNOWLEDGMENT

This material is based upon work supported primarily by the US Department of Energy, Office of Science, Office of Basic Energy Sciences, as part of the Energy Frontier Research Centers program: CSSAS--The Center for the Science of Synthesis Across Scales under Award Number DE-SC0019288. F.M. acknowledges postdoctoral fellowship support from the German Academic Exchange Service (DAAD) with funds from the German Federal Ministry of Education and Research (BMBF) and the European Union (FP7-PEOPLE-2013-COFUND - grant agreement n° 605728). Y. L. acknowledges support from the Office of Naval Research through Grant Number N00014-17-1-2201 for performing the ellipsometry measurements. Part of this work was conducted at the Molecular Analysis Facility, a National Nanotechnology Coordinated Infrastructure (NNCI) site at the University of Washington, which is supported in part by funds

from the National Science Foundation (awards NNCI-2025489, NNCI-1542101), the Molecular Engineering & Sciences Institute, and the Clean Energy Institute. We are thankful to Harrison J. Goldwyn, Kevin C. Smith, and David J. Masiello for insightful discussions.

## REFERENCES

- (1) Green, M. A.; Ho-Baillie, A.; Snaith, H. J. The Emergence of Perovskite Solar Cells. *Nat. Photonics* **2014**, *8* (7), 506–514. <https://doi.org/10.1038/nphoton.2014.134>.
- (2) Sun, S.; Salim, T.; Mathews, N.; Duchamp, M.; Boothroyd, C.; Xing, G.; Sum, T. C.; Lam, Y. M. The Origin of High Efficiency in Low-Temperature Solution-Processable Bilayer Organometal Halide Hybrid Solar Cells. *Energy Environ. Sci.* **2014**, *7* (1), 399–407. <https://doi.org/10.1039/C3EE43161D>.
- (3) Stranks, S. D.; Burlakov, V. M.; Leijtens, T.; Ball, J. M.; Goriely, A.; Snaith, H. J. Recombination Kinetics in Organic-Inorganic Perovskites: Excitons, Free Charge, and Subgap States. *Phys. Rev. Appl.* **2014**, *2* (3), 034007. <https://doi.org/10.1103/PhysRevApplied.2.034007>.
- (4) Shi, D.; Adinolfi, V.; Comin, R.; Yuan, M.; Alarousu, E.; Buin, A.; Chen, Y.; Hoogland, S.; Rothenberger, A.; Katsiev, K.; Losovyj, Y.; Zhang, X.; Dowben, P. A.; Mohammed, O. F.; Sargent, E. H.; Bakr, O. M. Low Trap-State Density and Long Carrier Diffusion in Organolead Trihalide Perovskite Single Crystals. *Science* **2015**, *347* (6221), 519–522. <https://doi.org/10.1126/science.aaa2725>.
- (5) Ji, K.; Anaya, M.; Abfalterer, A.; Stranks, S. D. Halide Perovskite Light-Emitting Diode Technologies. *Adv. Opt. Mater.* **2021**, *9*, 2002128. <https://doi.org/10.1002/adom.202002128>.
- (6) Li, J.; Duan, J.; Yang, X.; Duan, Y.; Yang, P.; Tang, Q. Review on Recent Progress of Lead-Free Halide Perovskites in Optoelectronic Applications. *Nano Energy* **2021**, *80*, 105526. <https://doi.org/10.1016/j.nanoen.2020.105526>.
- (7) Katan, C.; Mercier, N.; Even, J. Quantum and Dielectric Confinement Effects in Lower-Dimensional Hybrid Perovskite Semiconductors. *Chem. Rev.* **2019**, *119* (5), 3140–3192. <https://doi.org/10.1021/acs.chemrev.8b00417>.
- (8) Stoumpos, C. C.; Cao, D. H.; Clark, D. J.; Young, J.; Rondinelli, J. M.; Jang, J. I.; Hupp, J. T.; Kanatzidis, M. G. Ruddlesden–Popper Hybrid Lead Iodide Perovskite 2D Homologous Semiconductors. *Chem. Mater.* **2016**, *28* (8), 2852–2867. <https://doi.org/10.1021/acs.chemmater.6b00847>.
- (9) Blancon, J.-C.; Tsai, H.; Nie, W.; Stoumpos, C. C.; Pedesseau, L.; Katan, C.; Kepenekian, M.; Soe, C. M. M.; Appavoo, K.; Sfeir, M. Y.; Tretiak, S.; Ajayan, P. M.; Kanatzidis, M.

- G.; Even, J.; Crochet, J. J.; Mohite, A. D. Extremely Efficient Internal Exciton Dissociation through Edge States in Layered 2D Perovskites. *Science* **2017**, *355* (6331), 1288–1292. <https://doi.org/10.1126/science.aal4211>.
- (10) Straus, D. B.; Kagan, C. R. Electrons, Excitons, and Phonons in Two-Dimensional Hybrid Perovskites: Connecting Structural, Optical, and Electronic Properties. *J. Phys. Chem. Lett.* **2018**, *9* (6), 1434–1447. <https://doi.org/10.1021/acs.jpcclett.8b00201>.
- (11) Fieramosca, A.; De Marco, L.; Passoni, M.; Polimeno, L.; Rizzo, A.; Rosa, B. L. T.; Cruciani, G.; Dominici, L.; De Giorgi, M.; Gigli, G.; Andreani, L. C.; Gerace, D.; Ballarini, D.; Sanvitto, D. Tunable Out-of-Plane Excitons in 2D Single-Crystal Perovskites. *ACS Photonics* **2018**, *5* (10), 4179–4185. <https://doi.org/10.1021/acsp Photonics.8b00984>.
- (12) Zhang, Q.; Su, R.; Du, W.; Liu, X.; Zhao, L.; Ha, S. T.; Xiong, Q. Advances in Small Perovskite-Based Lasers. *Small Methods* **2017**, *1* (9), 1700163. <https://doi.org/10.1002/smt.201700163>.
- (13) Schlaus, A. P.; Spencer, M. S.; Zhu, X.-Y. Light–Matter Interaction and Lasing in Lead Halide Perovskites. *Acc. Chem. Res.* **2019**, *52* (10), 2950–2959. <https://doi.org/10.1021/acs.accounts.9b00382>.
- (14) Park, K.; Lee, J. W.; Kim, J. D.; Han, N. S.; Jang, D. M.; Jeong, S.; Park, J.; Song, J. K. Light–Matter Interactions in Cesium Lead Halide Perovskite Nanowire Lasers. *J. Phys. Chem. Lett.* **2016**, *7* (18), 3703–3710. <https://doi.org/10.1021/acs.jpcclett.6b01821>.
- (15) Carretero-Palacios, S.; Calvo, M. E.; Míguez, H. Absorption Enhancement in Organic-Inorganic Halide Perovskite Films with Embedded Plasmonic Gold Nanoparticles. *J. Phys. Chem. C* **2015**, *119* (32), 18635–18640. <https://doi.org/10.1021/acs.jpcc.5b06473>.
- (16) Li, H.; He, F.; Ji, C.; Zhu, W.; Xu, Y.; Zhang, W.; Meng, X.; Fang, X.; Ding, T. Purcell-Enhanced Spontaneous Emission from Perovskite Quantum Dots Coupled to Plasmonic Crystal. *J. Phys. Chem. C* **2019**, *123* (41), 25359–25365. <https://doi.org/10.1021/acs.jpcc.9b06919>.
- (17) Adl, H. P.; Gorji, S.; Habil, M. K.; Suárez, I.; Chirvony, V. S.; Gualdrón-Reyes, A. F.; Mora-Seró, I.; Valencia, L. M.; de la Mata, M.; Hernández-Saz, J.; Molina, S. I.; Zapata-Rodríguez, C. J.; Martínez-Pastor, J. P. Purcell Enhancement and Wavelength Shift of Emitted Light by CsPbI<sub>3</sub> Perovskite Nanocrystals Coupled to Hyperbolic Metamaterials. *ACS Photonics* **2020**, *7* (11), 3152–3160. <https://doi.org/10.1021/acsp Photonics.0c01219>.
- (18) Adamo, G.; Swaha Krishnamoorthy, H. N.; Cortecchia, D.; Chaudhary, B.; Nalla, V.; Zheludev, N. I.; Soci, C. Metamaterial Enhancement of Metal-Halide Perovskite Luminescence. *Nano Lett.* **2020**. <https://doi.org/10.1021/acs.nanolett.0c02571>.
- (19) Yang, Z.; Pelton, M.; Bodnarchuk, M. I.; Kovalenko, M. V.; Waks, E. Spontaneous Emission Enhancement of Colloidal Perovskite Nanocrystals by a Photonic Crystal Cavity. *Appl. Phys. Lett.* **2017**, *111* (22). <https://doi.org/10.1063/1.5000248>.

- (20) Zhang, X.; Shi, H.; Dai, H.; Zhang, X.; Sun, X. W.; Zhang, Z. Exciton-Polariton Properties in Planar Microcavity of Millimeter-Sized Two-Dimensional Perovskite Sheet. *ACS Appl. Mater. Interfaces* **2020**, *12* (4), 5081–5089. <https://doi.org/10.1021/acsami.9b19968>.
- (21) Du, W.; Zhang, S.; Zhang, Q.; Liu, X. Recent Progress of Strong Exciton–Photon Coupling in Lead Halide Perovskites. *Adv. Mater.* **2019**, *31* (45), 1–6. <https://doi.org/10.1002/adma.201804894>.
- (22) Fieramosca, A.; Polimeno, L.; Ardizzone, V.; De Marco, L.; Pugliese, M.; Maiorano, V.; De Giorgi, M.; Dominici, L.; Gigli, G.; Gerace, D.; Ballarini, D.; Sanvitto, D. Two-Dimensional Hybrid Perovskites Sustaining Strong Polariton Interactions at Room Temperature. *Sci. Adv.* **2019**, *5* (5), 1–7. <https://doi.org/10.1126/sciadv.aav9967>.
- (23) Shen, T.; Siontas, S.; Pacifici, D. Plasmon-Enhanced Thin-Film Perovskite Solar Cells. *J. Phys. Chem. C* **2018**, *122* (41), 23691–23697. <https://doi.org/10.1021/acs.jpcc.8b07063>.
- (24) Li, Y.-F.; Kou, Z.-L.; Feng, J.; Sun, H.-B. Plasmon-Enhanced Organic and Perovskite Solar Cells with Metal Nanoparticles. *Nanophotonics* **2020**, *9* (10), 3111–3133. <https://doi.org/10.1515/nanoph-2020-0099>.
- (25) Gu, L.; Wen, K.; Peng, Q.; Huang, W.; Wang, J. Surface-Plasmon-Enhanced Perovskite Light-Emitting Diodes. *Small* **2020**, *16* (30), 2001861. <https://doi.org/10.1002/smll.202001861>.
- (26) Su, R.; Diederichs, C.; Wang, J.; Liew, T. C. H.; Zhao, J.; Liu, S.; Xu, W.; Chen, Z.; Xiong, Q. Room-Temperature Polariton Lasing in All-Inorganic Perovskite Nanoplatelets. *Nano Lett.* **2017**, *17* (6), 3982–3988. <https://doi.org/10.1021/acs.nanolett.7b01956>.
- (27) Makarov, S.; Furasova, A.; Tiguntseva, E.; Hemmetter, A.; Berestennikov, A.; Pushkarev, A.; Zakhidov, A.; Kivshar, Y. Halide-Perovskite Resonant Nanophotonics. *Adv. Opt. Mater.* **2019**, *7* (1), 1800784. <https://doi.org/10.1002/adom.201800784>.
- (28) Su, R.; Ghosh, S.; Wang, J.; Liu, S.; Diederichs, C.; Liew, T. C. H.; Xiong, Q. Observation of Exciton Polariton Condensation in a Perovskite Lattice at Room Temperature. *Nat. Phys.* **2020**, *16* (3), 301–306. <https://doi.org/10.1038/s41567-019-0764-5>.
- (29) Pyles, H.; Zhang, S.; De Yoreo, J. J.; Baker, D. Controlling Protein Assembly on Inorganic Crystals through Designed Protein Interfaces. *Nature* **2019**, *571* (7764), 251–256. <https://doi.org/10.1038/s41586-019-1361-6>.
- (30) Zhao, Y.; Xu, C. DNA-Based Plasmonic Heterogeneous Nanostructures: Building, Optical Responses, and Bioapplications. *Adv. Mater.* **2020**, *32* (41), 1907880. <https://doi.org/10.1002/adma.201907880>.
- (31) Chen, Y.; Munechika, K.; Ginger, D. S. Dependence of Fluorescence Intensity on the Spectral Overlap between Fluorophores and Plasmon Resonant Single Silver Nanoparticles. *Nano Lett.* **2007**, *7* (3), 690–696. <https://doi.org/10.1021/nl062795z>.

- (32) Chen, J. I. L.; Chen, Y.; Ginger, D. S. Plasmonic Nanoparticle Dimers for Optical Sensing of DNA in Complex Media. *J. Am. Chem. Soc.* **2010**, *132* (28), 9600–9601. <https://doi.org/10.1021/ja103240g>.
- (33) Wang, B.; Yu, P.; Wang, W.; Zhang, X.; Kuo, H. C.; Xu, H.; Wang, Z. M. High-Q Plasmonic Resonances: Fundamentals and Applications. *Adv. Opt. Mater.* **2021**, *2001520*, 1–30. <https://doi.org/10.1002/adom.202001520>.
- (34) Miroshnichenko, A. E.; Flach, S.; Kivshar, Y. S. Fano Resonances in Nanoscale Structures. *Rev. Mod. Phys.* **2010**, *82* (3), 2257–2298. <https://doi.org/10.1103/RevModPhys.82.2257>.
- (35) Bekele, D.; Yu, Y.; Yvind, K.; Mork, J. In-Plane Photonic Crystal Devices Using Fano Resonances. *Laser Photon. Rev.* **2019**, *13* (12), 1900054. <https://doi.org/10.1002/lpor.201900054>.
- (36) Fano, U. Effects of Configuration Interaction on Intensities and Phase Shifts. *Phys. Rev.* **1961**, *124* (6), 1866–1878. <https://doi.org/10.1103/PhysRev.124.1866>.
- (37) Limonov, M. F.; Rybin, M. V.; Poddubny, A. N.; Kivshar, Y. S. Fano Resonances in Photonics. *Nat. Photonics* **2017**, *11* (9), 543–554. <https://doi.org/10.1038/NPHOTON.2017.142>.
- (38) Pelton, M.; Storm, S. D.; Leng, H. Strong Coupling of Emitters to Single Plasmonic Nanoparticles: Exciton-Induced Transparency and Rabi Splitting. *Nanoscale* **2019**, *11* (31), 14540–14552. <https://doi.org/10.1039/C9NR05044B>.
- (39) Liu, N.; Liedl, T. DNA-Assembled Advanced Plasmonic Architectures. *Chem. Rev.* **2018**, *118* (6), 3032–3053. <https://doi.org/10.1021/acs.chemrev.7b00225>.
- (40) Thakkar, N.; Rea, M. T.; Smith, K. C.; Heylman, K. D.; Quillin, S. C.; Knapper, K. A.; Horak, E. H.; Masiello, D. J.; Goldsmith, R. H. Sculpting Fano Resonances to Control Photonic-Plasmonic Hybridization. *Nano Lett.* **2017**, *17* (11), 6927–6934. <https://doi.org/10.1021/acs.nanolett.7b03332>.
- (41) Pan, F.; Smith, K. C.; Nguyen, H. L.; Knapper, K. A.; Masiello, D. J.; Goldsmith, R. H. Elucidating Energy Pathways through Simultaneous Measurement of Absorption and Transmission in a Coupled Plasmonic-Photonic Cavity. *Nano Lett.* **2020**, *20* (1), 50–58. <https://doi.org/10.1021/acs.nanolett.9b02796>.
- (42) Luk'yanchuk, B.; Zheludev, N. I.; Maier, S. A.; Halas, N. J.; Nordlander, P.; Giessen, H.; Chong, C. T. The Fano Resonance in Plasmonic Nanostructures and Metamaterials. *Nat. Mater.* **2010**, *9* (9), 707–715. <https://doi.org/10.1038/nmat2810>.
- (43) Sugawara, Y.; Kelf, T. A.; Baumberg, J. J.; Abdelsalam, M. E.; Bartlett, P. N. Strong Coupling between Localized Plasmons and Organic Excitons in Metal Nanovoids. *Phys. Rev. Lett.* **2006**, *97* (26), 266808. <https://doi.org/10.1103/PhysRevLett.97.266808>.
- (44) Sonnefraud, Y.; Verellen, N.; Sobhani, H.; Vandenbosch, G. A. E.; Moshchalkov, V. V;

- Van Dorpe, P.; Nordlander, P.; Maier, S. A. Experimental Realization of Subradiant, Superradiant, and Fano Resonances in Ring/Disk Plasmonic Nanocavities. *ACS Nano* **2010**, *4* (3), 1664–1670. <https://doi.org/10.1021/nn901580r>.
- (45) Liu, W.; Lee, B.; Naylor, C. H.; Ee, H.-S.; Park, J.; Johnson, A. T. C.; Agarwal, R. Strong Exciton–Plasmon Coupling in MoS<sub>2</sub> Coupled with Plasmonic Lattice. *Nano Lett.* **2016**, *16* (2), 1262–1269. <https://doi.org/10.1021/acs.nanolett.5b04588>.
- (46) Shang, Q.; Zhang, S.; Liu, Z.; Chen, J.; Yang, P.; Li, C.; Li, W.; Zhang, Y.; Xiong, Q.; Liu, X.; Zhang, Q. Surface Plasmon Enhanced Strong Exciton–Photon Coupling in Hybrid Inorganic–Organic Perovskite Nanowires. *Nano Lett.* **2018**, *18* (6), 3335–3343. <https://doi.org/10.1021/acs.nanolett.7b04847>.
- (47) Zhang, S.; Shang, Q.; Du, W.; Shi, J.; Wu, Z.; Mi, Y.; Chen, J.; Liu, F.; Li, Y.; Liu, M.; Zhang, Q.; Liu, X. Strong Exciton-Photon Coupling in Hybrid Inorganic-Organic Perovskite Micro/Nanowires. *Adv. Opt. Mater.* **2018**, *6* (2), 1701032. <https://doi.org/10.1002/adom.201701032>.
- (48) Schünemann, S.; Brittman, S.; Chen, K.; Garnett, E. C.; Tüysüz, H. Halide Perovskite 3D Photonic Crystals for Distributed Feedback Lasers. *ACS Photonics* **2017**, *4* (10), 2522–2528. <https://doi.org/10.1021/acsp Photonics.7b00780>.
- (49) Hou, S.; Xie, A.; Xie, Z.; Tobing, L. Y. M.; Zhou, J.; Tjahjana, L.; Yu, J.; Hettiarachchi, C.; Zhang, D.; Dang, C.; Teo, E. H. T.; Birowosuto, M. D.; Wang, H. Concurrent Inhibition and Redistribution of Spontaneous Emission from All Inorganic Perovskite Photonic Crystals. *ACS Photonics* **2019**, *6* (6), 1331–1337. <https://doi.org/10.1021/acsp Photonics.8b01655>.
- (50) Huang, C.; Zhang, C.; Xiao, S.; Wang, Y.; Fan, Y.; Liu, Y.; Zhang, N.; Qu, G.; Ji, H.; Han, J.; Ge, L.; Kivshar, Y.; Song, Q. Ultrafast Control of Vortex Microlasers. *Science* **2020**, *367* (6481), 1018–1021. <https://doi.org/10.1126/science.aba4597>.
- (51) Sun, W.; Liu, Y.; Qu, G.; Fan, Y.; Dai, W.; Wang, Y.; Song, Q.; Han, J.; Xiao, S. Lead Halide Perovskite Vortex Microlasers. *Nat. Commun.* **2020**, *11* (1). <https://doi.org/10.1038/s41467-020-18669-1>.
- (52) Fan, Y.; Wang, Y.; Zhang, N.; Sun, W.; Gao, Y.; Qiu, C.; Song, Q.; Xiao, S. Resonance-Enhanced Three-Photon Luminescence via Lead Halide Perovskite Metasurfaces for Optical Encoding. *Nat. Commun.* No. 2019, 1–8. <https://doi.org/10.1038/s41467-019-10090-7>.
- (53) Li, Z.; Smalley, J. S. T.; Haroldson, R.; Lin, D.; Hawkins, R.; Gharajeh, A.; Moon, J.; Hou, J.; Zhang, C.; Hu, W.; Zakhidov, A.; Gu, Q. Active Perovskite Hyperbolic Metasurface. *ACS Photonics* **2020**, *7* (7), 1754–1761. <https://doi.org/10.1021/acsp Photonics.0c00391>.
- (54) Franceschini, P.; Carletti, L.; Pushkarev, A. P.; Preda, F.; Perri, A.; Tognazzi, A.; Ronchi, A.; Ferrini, G.; Pagliara, S.; Banfi, F.; Polli, D.; Cerullo, G.; De Angelis, C.; Makarov, S. V.; Giannetti, C. Tuning the Ultrafast Response of Fano Resonances in Halide Perovskite Nanoparticles. *ACS Nano* **2020**, *14* (10), 13602–13610.

<https://doi.org/10.1021/acsnano.0c05710>.

- (55) Stoddard, R. J.; Dunlap-Shohl, W. A.; Qiao, H.; Meng, Y.; Kau, W. F.; Hillhouse, H. W. Forecasting the Decay of Hybrid Perovskite Performance Using Optical Transmittance or Reflected Dark-Field Imaging. *ACS Energy Lett.* **2020**, *5* (3), 946–954. <https://doi.org/10.1021/acsenerylett.0c00164>.
- (56) Schwarz, L.; Cartarius, H.; Wunner, G.; Heiss, W. D.; Main, J. Fano Resonances in Scattering: An Alternative Perspective. *Eur. Phys. J. D* **2015**, *69* (8), 1–4. <https://doi.org/10.1140/epjd/e2015-60202-9>.
- (57) Rybin, M. V.; Khanikaev, A. B.; Inoue, M.; Samusev, K. B.; Steel, M. J.; Yushin, G.; Limonov, M. F. Fano Resonance between Mie and Bragg Scattering in Photonic Crystals. *Phys. Rev. Lett.* **2009**, *103* (2), 1–4. <https://doi.org/10.1103/PhysRevLett.103.023901>.
- (58) Thakkar, N.; Rea, M. T.; Smith, K. C.; Heylman, K. D.; Quillin, S. C.; Knapper, K. A.; Horak, E. H.; Masiello, D. J.; Goldsmith, R. H. Sculpting Fano Resonances To Control Photonic–Plasmonic Hybridization. *Nano Lett.* **2017**, *17* (11), 6927–6934. <https://doi.org/10.1021/acs.nanolett.7b03332>.
- (59) Wu, X.; Gray, S. K.; Pelton, M. Quantum-Dot-Induced Transparency in a Nanoscale Plasmonic Resonator. *Opt. Express* **2010**, *18* (23), 23633. <https://doi.org/10.1364/OE.18.023633>.
- (60) Zengin, G.; Johansson, G.; Johansson, P.; Antosiewicz, T. J.; Käll, M.; Shegai, T. Approaching the Strong Coupling Limit in Single Plasmonic Nanorods Interacting with J-Aggregates. *Sci. Rep.* **2013**, *3* (1), 3074. <https://doi.org/10.1038/srep03074>.
- (61) Tiguntseva, E. Y.; Baranov, D. G.; Pushkarev, A. P.; Munkhbat, B.; Komissarenko, F.; Franckevičius, M.; Zakhidov, A. A.; Shegai, T.; Kivshar, Y. S.; Makarov, S. V. Tunable Hybrid Fano Resonances in Halide Perovskite Nanoparticles. *Nano Lett.* **2018**, *18* (9), 5522–5529. <https://doi.org/10.1021/acs.nanolett.8b01912>.
- (62) Cai, C.; Bi, G.; Xu, T. Fano Resonance in the CsPbBr<sub>3</sub> Nanocrystal/Ag Nanostructure through the Exciton-Plasmon Coupling. *Appl. Phys. Lett.* **2019**, *115* (16), 161602. <https://doi.org/10.1063/1.5124408>.
- (63) Chen, J.; Zhang, Q.; Shi, J.; Zhang, S.; Du, W.; Mi, Y.; Shang, Q.; Liu, P.; Sui, X.; Wu, X.; Wang, R.; Peng, B.; Zhong, H.; Xing, G.; Qiu, X.; Sum, T. C.; Liu, X. Room Temperature Continuous-Wave Excited Biexciton Emission in Perovskite Nanoplatelets via Plasmonic Nonlinear Fano Resonance. *Commun. Phys.* **2019**, *2* (1), 80. <https://doi.org/10.1038/s42005-019-0178-9>.
- (64) Xue, C.; Mirkin, C. A. PH-Switchable Silver Nanoprism Growth Pathways. *Angew. Chemie Int. Ed.* **2007**, *46* (12), 2036–2038. <https://doi.org/10.1002/anie.200604637>.
- (65) Jin, R.; Charles Cao, Y.; Hao, E.; Métraux, G. S.; Schatz, G. C.; Mirkin, C. A. Controlling Anisotropic Nanoparticle Growth through Plasmon Excitation. *Nature* **2003**, *425* (6957),

- 487–490. <https://doi.org/10.1038/nature02020>.
- (66) Kulkarni, A. P.; Munechika, K.; Noone, K. M.; Smith, J. M.; Ginger, D. S. Phase Transfer of Large Anisotropic Plasmon Resonant Silver Nanoparticles from Aqueous to Organic Solution. *Langmuir* **2009**, *25* (14), 7932–7939. <https://doi.org/10.1021/la900600z>.
- (67) Antosiewicz, T. J.; Apell, S. P.; Shegai, T. Plasmon–Exciton Interactions in a Core–Shell Geometry: From Enhanced Absorption to Strong Coupling. *ACS Photonics* **2014**, *1* (5), 454–463. <https://doi.org/10.1021/ph500032d>.
- (68) Houdré, R. Early Stages of Continuous Wave Experiments on Cavity-Polaritons. *Phys. status solidi* **2005**, *242* (11), 2167–2196. <https://doi.org/10.1002/pssb.200560966>.
- (69) Luo, Y.; Zhao, J. Plasmon-Exciton Interaction in Colloidally Fabricated Metal Nanoparticle-Quantum Emitter Nanostructures. *Nano Res.* **2019**, *12* (9), 2164–2171. <https://doi.org/10.1007/s12274-019-2390-z>.
- (70) Wen, J.; Wang, H.; Wang, W.; Deng, Z.; Zhuang, C.; Zhang, Y.; Liu, F.; She, J.; Chen, J.; Chen, H.; Deng, S.; Xu, N. Room-Temperature Strong Light–Matter Interaction with Active Control in Single Plasmonic Nanorod Coupled with Two-Dimensional Atomic Crystals. *Nano Lett.* **2017**, *17* (8), 4689–4697. <https://doi.org/10.1021/acs.nanolett.7b01344>.
- (71) Stührenberg, M.; Munkhbat, B.; Baranov, D. G.; Cuadra, J.; Yankovich, A. B.; Antosiewicz, T. J.; Olsson, E.; Shegai, T. Strong Light–Matter Coupling between Plasmons in Individual Gold Bi-Pyramids and Excitons in Mono- and Multilayer WSe<sub>2</sub>. *Nano Lett.* **2018**, *18* (9), 5938–5945. <https://doi.org/10.1021/acs.nanolett.8b02652>.
- (72) Geisler, M.; Cui, X.; Wang, J.; Rindzevicius, T.; Gammelgaard, L.; Jessen, B. S.; Gonçalves, P. A. D.; Todisco, F.; Bøggild, P.; Boisen, A.; Wubs, M.; Mortensen, N. A.; Xiao, S.; Stenger, N. Single-Crystalline Gold Nanodisks on WS<sub>2</sub> Mono- and Multilayers for Strong Coupling at Room Temperature. *ACS Photonics* **2019**, *6* (4), 994–1001. <https://doi.org/10.1021/acsp Photonics.8b01766>.
- (73) Wang, H.; Wen, J.; Wang, W.; Xu, N.; Liu, P.; Yan, J.; Chen, H.; Deng, S. Resonance Coupling in Heterostructures Composed of Silicon Nanosphere and Monolayer WS<sub>2</sub>: A Magnetic-Dipole-Mediated Energy Transfer Process. *ACS Nano* **2019**, *13* (2), 1739–1750. <https://doi.org/10.1021/acsnano.8b07826>.
- (74) Munkhbat, B.; Baranov, D. G.; Bisht, A.; Hoque, M. A.; Karpiak, B.; Dash, S. P.; Shegai, T. Electrical Control of Hybrid Monolayer Tungsten Disulfide–Plasmonic Nanoantenna Light–Matter States at Cryogenic and Room Temperatures. *ACS Nano* **2020**, *14* (1), 1196–1206. <https://doi.org/10.1021/acsnano.9b09684>.
- (75) *Handbook of Optical Constants of Solids*; Palik, E. D., Ed.; Elsevier, 1985.
- (76) Li, G.-C.; Zhang, Q.; Maier, S. A.; Lei, D. Plasmonic Particle-on-Film Nanocavities: A Versatile Platform for Plasmon-Enhanced Spectroscopy and Photochemistry. *Nanophotonics* **2018**, *7* (12), 1865–1889. <https://doi.org/10.1515/nanoph-2018-0162>.

- (77) Jin, R.; Cao, Y.; Mirkin, C. A.; Kelly, K. L.; Schatz, G. C.; Zheng, J. G. Photoinduced Conversion of Silver Nanospheres to Nanoprisms. *Science* **2001**, *294* (5548), 1901–1903. <https://doi.org/10.1126/science.1066541>.
- (78) Chikkaraddy, R.; De Nijs, B.; Benz, F.; Barrow, S. J.; Scherman, O. A.; Rosta, E.; Demetriadou, A.; Fox, P.; Hess, O.; Baumberg, J. J. Single-Molecule Strong Coupling at Room Temperature in Plasmonic Nanocavities. *Nature* **2016**, *535* (7610), 127–130. <https://doi.org/10.1038/nature17974>.

## TOC graphic

### Light-Matter Coupling Mediated by Grain Structure

